

Numerical Studies of the Kelvin-Helmholtz Instability in the Coronal Jet

Tianle Zhao^{1,2,3}, Lei Ni^{1,3}, Jun Lin^{1,3} and Udo Ziegler⁴

¹ Yunnan Observatories, Chinese Academy of Sciences, Kunming, Yunnan 650216, China;

leini@ynao.ac.cn

² University of Chinese Academy of Sciences, Yuquan Road, Shijingshan Block Beijing 100049, China;

³ Center for Astronomical Mega-Science, Chinese Academy of Sciences, 20A Datun Road, Chaoyang District, Beijing, 100012, China;

⁴ Leibniz-Lnstitut für Astrophysik Potsdam, Potsdam D-14482, Germany;

Abstract The Kelvin-Helmholtz (K-H) instability in the corona EUV jet is studied via 2.5 MHD numerical simulations. The jet results from magnetic reconnection due to the interaction of the new emerging magnetic field and the pre-existing magnetic field in the corona. Our results show that the Alfvén Mach number along the jet is about 5-14 just before the instability occurs, and it is even higher than 14 at some local areas. During the K-H instability process, several vortex-like plasma blobs of high temperature and high density appear along the jet, and magnetic fields have also been rolled up and the magnetic configuration including anti-parallel magnetic fields forms, which leads to magnetic reconnection at many X-points and current sheet fragments inside the vortex-like blob. After magnetic islands appear inside the main current sheet, the total kinetic energy of the reconnection outflows decreases, and cannot support the formation of the vortex-like blob along the jet any longer, then the K-H instability eventually disappears. We also present the results about how the guide field and the flux emerging speed affect the K-H instability. We find that the strong guide field inhibits the shock formation in the reconnection upward outflow regions but helps secondary magnetic islands appear earlier in

the main current sheet, and then apparently suppresses the K-H instability. As the speed of the emerging magnetic field decreases, the K-H instability appears later, the highest temperature inside the vortex blob gets lower and the vortex structure gets smaller.

Key words: Sun: corona jet, K-H instability, guide-field, method: Numerical simulations

1 INTRODUCTION

The jet that behaves as a transient phenomenon is ubiquitous in the solar atmosphere. It usually appears in the active region and in the polar corona hole. Jets are considered as the important mass and energy source of the upper solar atmosphere and solar wind Raouafi et al. (2016). They are usually observed in multiple wavelengths, such as $H\alpha$, Ca II H, EUV and soft X-ray (e.g., Roy & Tang, 1975; Shibata et al., 2007; Alexander & Fletcher, 1999; Shen et al., 2011; Shibata et al., 1992), and their dynamic, thermal, and structural behaviours are different when observed in different wavelengths, which can be used to explore the possible mechanisms of the jet. Coronal jets are usually observed in EUV and X-ray wavelengths. Raouafi et al. (2016) summarized the characteristics of the corona jet according to their manifestations, such as the velocity, width, height, lifetime and temperature. The temperature of EUV jets ranges from 0.1 to 10 MK, and the X-ray jets can be hotter than 10 MK. Moore et al. (2010) divided the jet into the standard and the blow-out jets according to their morphological features. The spire of the standard jet is narrow during its entire lifetime and the base is relatively dim. The standard jet are modeled by Shibata et al. (1992). The spires of the blow-out jets on the other hand become broader with time and eventually reach the size comparable to the width of the jet base, the brightening of the arch base is apparent, the twist and the shearing motions usually appear in the event. Both the standard jet and the blow-out jet are considered to be resulted from magnetic reconnection between the emerging new magnetic field and the pre-existing coronal magnetic field.

As the resolution of solar telescopes are improved, many fine structures in the jet have been observed. Zhang & Ji (2014) and Zhang et al. (2016) analyzed the EUV data from Solar Terrestrial Relations Observatory (STEREO) and the Atmospheric Imaging Assembly on the Solar Dynamics Observatory (SDO), they found that the bright blobs were produced and ejected out along the jets. The lifetime of these blobs is about 24–60 s, the temperature is between 0.5 MK and 4 MK, and the

diameter ranges from 2 to 10 Mm. Zhang & Zhang (2017) recognized multiple upward and downward bright blobs in the legs of the jet via studying the high-resolution data from Interface Region Imaging Spectrograph (IRIS). Recently, several observations also show the detailed studies about the bright blobs in the corona jets (e.g. Li et al., 2017; Shen et al., 2017). The mechanism of the blob formation in coronal jets is mainly considered as the plasmoid instability (e.g., Bhattacharjee et al., 2009; Ni et al., 2013; Comisso & Bhattacharjee, 2016; Nemati et al., 2017) in the magnetic reconnection process. In previous two-dimensional and three-dimensional simulations (e.g., Jiang et al., 2012; Yang et al., 2013; Moreno-Insertis & Galsgaard, 2013; Wyper et al., 2016) the high density magnetic island or magnetic flux rope (3D) were found to form in the magnetic reconnection process when the Lundquist number was high enough. These magnetic island or magnetic flux rope (3D) are believed to correspond to the observed bright blobs.

However, the magnetic island or magnetic flux rope (3D) always merged into the background magnetic fields and the plasma in these simulations, none of them was observed to be ejected out along the jet as shown in the observational results of Zhang & Ji (2014) and Zhang et al. (2016). For the first time, recent high resolution numerical experiments with high Lundquist number by Ni et al. (2017) indicated that the magnetic island can be easily formed and ejected out along the jet when the plasma β is low enough. The characteristics of the magnetic island is similar to that of bright blobs observed in the EUV band. In the case with higher plasma β , the K-H instability appeared along the jet and resulted in the vortex-like high density and high temperature blobs, which was suggestive of accounting for the bright blob observed in the EUV band.

K-H instability was found on the shear plane with relative motions between two fluids by Kelvin(1871) and Helmholtz(1868) one and a half centuries ago. But only a small number of observations have shown the K-H instability on the Sun. The irregular evolution of a CME was analyzed by Foullon et al. (2013), they inferred that the characteristics of the evolutionary process were consistent with the result of the K-H instability. When studying an eruption that started from an active region and produced a CME and flare, Ofman & Thompson (2011) noticed for the first time that the K-H instability occurring in the eruption magnetic configuration. They found a set of vortices at the interface between the region where the eruption took place and the nearby region. The sizes of these vortices varied from a few to ten arcseconds and the speed of these features on the interface ranged from 6 to 14 km/s.

Ofman & Thompson (2011) identified the vortices with the consequence of the K-H instability, which was confirmed by their linear analysis and nonlinear 2.5-MHD numerical experiment. They concluded that it is the velocity shearing between the erupting and the nearby stationary magnetic configuration that drove the instability.

Kuridze et al. (2016) found that some of the small-scale structures in the chromospheric jet displayed apparent red and blue shift in the spectral lines and that the vortex-like structures rapidly appeared along the boundary of the jet. On the basis of the spectral analysis, they found that the chromospheric spectral lines became broader inside these vortex-like and turbulent structures, which could be ascribed to the K-H instability. Zaqarashvili et al. (2015) compared the results of their theoretical model with those of observations, and found that when the jet speed was higher than the Alfvén speed in the jet direction, the K-H instability may happen. So far, both theory and observations indicate that the K-H instability is not easy to happen in the X-ray jets with high speed and low plasma density, but it is easier to appear in the EUV jets with lower speed and higher plasma density.

Some studies about the basic theories and numerical simulations of the K-H instability in the case with magnetic fields along the shearing flows have been reported. In the simulations by Jones et al. (1997) and Jeong et al. (2000), the K-H vortices were found to persist until the viscosity and small-scale reconnection dissipated them when the plasma β was high enough ($\beta = 3000$ & $\beta = 24000$) and the magnetic field was weak. Keppens et al. (1999) found that in a uniform magnetic field, the K-H mode grew between two shearing flows with time when the Alfvén Mach number $M_A = 9$, but it was stabilized when $M_A = 1.5$.

Tian & Chen (2016) numerically explored the K-H instability in the case of different magnetic fields imposed in the direction of the two shearing flows. The results showed that the dynamic behaviours of the plasma fluid change with the Alfvén Mach number in the direction of the fluid velocity. The K-H mode was linearly stabilized for $M_A \leq 2.27$; the K-H mode was nonlinearly stable and developed into wavy motions for $2.27 \leq M_A \leq 2.8$; in the range of $2.8 \leq M_A \leq 6.2$, the K-H mode was unstable and evolved into filamentary flows; the K-H vortex can fully roll up in an even higher M_A , e.g. $M_A = 50$, but the small-scale reconnection would destroy the K-H instability soon. The K-H instability has not

been identified in the previous corona EUV jet simulations except for the work by Ni et al. (2017).

In this work, we study the K-H instability in the solar coronal jet with different guide fields based on the previous 2D work by Ni et al. (2017). The effects of guide-field and flux emerging speed on the jet formation and K-H instability process will be presented. The numerical model is described in Section 2. We will present our numerical results in Section 3. In the last section, we will summary this work.

2 NUMERICAL MODEL

The single-fluid MHD equations including the gravity and the thermal conduction are given below:

$$\partial_t \rho = -\nabla \cdot (\rho \mathbf{v}), \quad (1)$$

$$\partial_t \mathbf{B} = \nabla \times (\mathbf{v} \times \mathbf{B} - \eta \nabla \times \mathbf{B}), \quad (2)$$

$$\begin{aligned} \partial_t (\rho \mathbf{v}) = & -\nabla \cdot \left[\rho \mathbf{v} \mathbf{v} + \left(p + \frac{1}{2\mu_0} |\mathbf{B}|^2 \right) \mathbf{I} \right] \\ & + \nabla \cdot \left[\frac{1}{\mu_0} \mathbf{B} \mathbf{B} \right] + \rho \mathbf{g}, \end{aligned} \quad (3)$$

$$\begin{aligned} \partial_t e = & -\nabla \cdot \left[\left(e + p + \frac{1}{2\mu_0} |\mathbf{B}|^2 \right) \mathbf{v} \right] \\ & + \nabla \cdot \left[\frac{1}{\mu_0} (\mathbf{v} \cdot \mathbf{B}) \mathbf{B} \right] + \nabla \cdot \left[\frac{\eta}{\mu_0} \mathbf{B} \times (\nabla \times \mathbf{B}) \right] \\ & - \nabla \cdot \mathbf{F}_C + \rho \mathbf{g} \cdot \mathbf{v}, \end{aligned} \quad (4)$$

$$e = \frac{p}{\Gamma_0 - 1} + \frac{1}{2} \rho |\mathbf{v}|^2 + \frac{1}{2\mu_0} |\mathbf{B}|^2, \quad (5)$$

$$p = \frac{2\rho}{m_i} k_B T. \quad (6)$$

Here, ρ , \mathbf{v} , e , \mathbf{B} and p represent the plasma density, velocity, the total energy density, the magnetic field and the gas pressure respectively. \mathbf{F}_C is the flux of the thermal conduction. $\mathbf{g} = -273.9 \text{ m s}^{-2} \mathbf{e}_y$ is the constant acceleration of gravity of the Sun. In this work, we use the international system of units (SI) for all the variables.

The initial background magnetic field is set as $B_{x0} = -0.6b_0$ and $B_{y0} = -0.8b_0$ ($b_0 = 0.0015$ T). In this work, we have added different guide fields in the z -direction for four cases: $B_{z0} = 0.05b_0$ in case I, III and IV and $B_{z0} = b_0$ in Case II. The initial plasma velocity is zero, and the initial temperature is $T_0 = 8 \times 10^5$ K. The initial stratified density including the constant acceleration of gravity is given as

$$\rho_0 = \rho_{00} \exp\left(-\frac{m_i g}{2k_B T_0} y\right) \quad (7)$$

where $\rho_{00} = 0.5 \times 1.66057 \times 10^{-10}$ kg m⁻³, the mass of proton is $m_i = 1.66057 \times 10^{-27}$ kg and the Boltzmann constant is $k_B = 1.3806 \times 10^{-23}$ J K⁻¹. The simulation box is inside the domain $0 < x < 200L_0$ and $0 < y < 100L_0$, with $L_0 = 10^6$ m.

We use the temperature-dependent magnetic diffusivity in all the four cases:

$$\eta = 10^8 (T_0/T)^{3/2} + 10^9 \left[1 - \tanh\left(\frac{y - 2L_0}{0.2L_0}\right)\right]. \quad (8)$$

Unit of η is m² s⁻¹. The anisotropic heat conduction flux, \mathbf{F}_C , is given by (e.g., see also Spitzer 1962):

$$\mathbf{F}_C = -\kappa_{\parallel} (\nabla T \cdot \hat{\mathbf{B}}) \hat{\mathbf{B}} - \kappa_{\perp} \left[\nabla T - (\nabla T \cdot \hat{\mathbf{B}}) \hat{\mathbf{B}} \right], \quad (9)$$

where $\hat{\mathbf{B}} = \mathbf{B}/|\mathbf{B}|$ is the unit vector in the direction of the magnetic field. The parallel and perpendicular thermal conductivity ratio, κ_{\parallel} and κ_{\perp} , are given by:

$$\kappa_{\parallel} = \frac{1.84 \times 10^{-10}}{\ln \Lambda} T^{5/2}, \quad (10)$$

$$\kappa_{\perp} = \min(\kappa'_{\perp}, \kappa_{\parallel}), \quad (11)$$

with

$$\kappa'_{\perp} = 8.04 \times 10^{-33} \left(\frac{\ln \Lambda}{m_i}\right)^2 \frac{\rho^2}{T^3 B^2} \kappa_{\parallel},$$

where $\ln \Lambda = 30$, unit for κ_{\parallel} and κ_{\perp} are J K⁻¹ m⁻¹ s⁻¹.

We use the NIRVANA code to solve equations (1) through (11) in this work. This code has been clearly described in previous works (e.g., Ziegler, 2008, 2011; Ni et al., 2017). The adaptive mesh refinement method in this simulation is the same as in the paper by Ni et al. (2017), the base-level grid is 320×160 , the highest refinement level is 10. All the pictures presented in this work are also plotted by using the level 3 or level 4 uniform IDL data, which are transformed from the original raw data.

Two extra layers with the ghost grid cell are applied to the code to set boundary conditions at each boundary. The boundary conditions are the same as in the previous paper by Ni et al. (2017) except that we also need to set boundary conditions for magnetic field and velocity in z -direction in this work. The outflow boundary conditions as described in Ni et al. (2017) are applied at the left ($x = 0$), right ($x = 200L_0$) and up ($y = 100L_0$) boundaries. The condition of divergence-free of the magnetic field requires the continuity of the normal component of the magnetic field on the boundary, which can be used to extrapolate the normal component through the boundary. We also insert two ghost layers below the physical bottom boundary $y = 0$. The gradient of the plasma velocity vanishes at the bottom boundary. The magnetic field inside the two layers with the ghost grid cells are set as:

$$b_{xb} = -0.6b_0 + \frac{100L_0(y - y_0)b_1f}{[(x - x_0)^2 + (y - y_0)^2]} \left[\tanh\left(\frac{x - 70L_0}{\lambda}\right) - \tanh\left(\frac{x - 130L_0}{\lambda}\right) \right], \quad (12)$$

$$b_{yb} = -0.8b_0 - \frac{100L_0(x - x_0)b_1f}{[(x - x_0)^2 + (y - y_0)^2]} \left[\tanh\left(\frac{x - 70L_0}{\lambda}\right) - \tanh\left(\frac{x - 130L_0}{\lambda}\right) \right], \quad (13)$$

where $f = t/t_1$ for $t \leq t_1$ and $f = 1$ for $t \geq t_1$, $x_0 = 100L_0$, $y_0 = -12L_0$, $b_1 = 3 \times 10^{-4}$ T and $\lambda = 0.5L_0$ with $t_1 = 500$ s for Cases I and II, $t_1 = 700$ s for Case III, and $t_1 = 350$ s for Case IV, respectively. We set the magnetic field in the z -direction in the bottom ghost grid cells b_{zb} to equal to the initial value of the magnetic field in the z -direction inside the computational domain, $b_{zb} = B_{z0}$. When $t < t_1$, the strength of the magnetic field below the bottom boundary varies with time, flux emerging stops after $t = t_1$. As shown previously by Forbes & Priest (1984), Chen & Shibata (2000), and Ding et al. (2010), one can set up the magnetic flux emergence by changing the conditions with time at the bottom boundary. As described by Ni et al. (2017), the magnetic field does not fulfill the divergence free condition $\nabla \cdot \mathbf{B} = 0$ inside the two ghost layers around $x = 70L_0$ and $x = 130L_0$.

The high magnetic diffusion below $y = 0.2L_0$ as shown in equation (8) can smooth the non-physical features inside the two ghost layers, then the related values at the bottom boundary are smoothed.

3 NUMERICAL RESULTS

3.1 K-H instability in corona jet with guide field

Case I and Case II differ from each other in the guide field. The guide field is $B_{z0} = 0.05b_0$ for Case I, and $B_{z0} = b_0$ for Case II. In Figures 1 and 2 we can see the distribution of the current density in z -direction J_z , the temperature T , the plasma density n , and the velocity along the jet direction $v_{||}$ and the distributions of the emission count rate in the AIA 211 Å channel at five different times in Cases I and II, from which we can see the jet evolutionary process in the two cases after the emergence of magnetic field stops. The distributions of each variable in Case I as shown in Figure 1 are almost the same as those displayed in Figure 7 of Ni et al. (2017). The jet lifetime is about 37 minutes, the jet maximum temperature is about 1.8 MK, and the maximum velocity along the jet direction is 320 km s^{-1} .

In Case II, the jet lifetime is about 33 mins, the maximum temperature is 1.6 MK, and the maximum velocity along the direction is 275 km s^{-1} , which are smaller than the corresponding parameters in Case I. In Figure 3, we presented the maximum velocities along the jet direction at each time step in all the four cases. One can see that there is an apparent peak in Cases I, III and IV with weak guide field, these peaks appear after the K-H instability starts and before the magnetic island appears in each of these case. However, there is no apparent peak in Case II with strong guide field. The maximum velocity along the jet direction in Case II is also slightly smaller than that in Case I after K-H instability appears. We notice that the characteristics of the simulated jets here are consistent with those showed by EUV observations of corona jets (see Raouafi et al. 2016).

In Figures 1 and 2, we can see clearly that the vortex-like blobs with high density and high temperature are rolled up in the jet. The vortex-like structure of the plasma blob at the bottom of the jet is more apparent than those at the higher positions of the jet. The higher the plasma blob is, the less the blob is rolled up. As pointed out by Ni et al. (2017), these vortex-like blobs indicate the strong shearing flows between the the surrounding plasma and jet, which leads to the K-H instability.

Based on the previous theory and simulations (e.g., Keppens et al., 1999; Tian & Chen, 2016), the K-H instability can be suppressed by the magnetic field along the shearing layers, and it can only appear when the Alfvén Mach number along the shearing layers is high enough. Figure 4 shows the distribution of velocity $v_{||}$ and the corresponding Alfvén Mach number, M_A , at $t = 784.3$ s before K-H instability happens. $v_{||}$ is the plasma velocity along the jet direction. From Figure 4, we can find that the jet direction is roughly the same as the direction of the initial background magnetic fields in the xy - plane at $t = 784.3$ s. Though the maximum of $v_{||}$ is only 265 km s^{-1} , which is still larger than the corresponding Alfvén velocity $v_{A||}$ along the jet. The Alfvén Mach number along the jet direction is defined as $M_A = v_{||}/v_{A||}$ (e.g., Keppens et al., 1999; Tian & Chen, 2016), and the value of M_A is between 5 and 14 in most regions inside the jet. In this work, we use the strength of magnetic field component which is parallel to the jet direction to calculate the Alfvén speed $v_{A||}$. From Figure 4 we can also find that M_A is apparently larger than 14 at some local areas, the magnetic fields are strongly folded and almost perpendicular to the jet direction at these areas. Therefore, the Alfvén velocity $v_{A||}$ along the jet is close to zero and M_A is very large in these areas.

Keppens et al. (1999) studied the K-H instability by using different initial magnetic configurations around the shearing flows. In the cases that parallel magnetic fields at both sides of the flows possess the same orientation, they found that the K-H instability grew with time when the initial Alfvén Mach number was $M_A = 9$, and it was stabilized when the magnetic field was strong and $M_A = 1.5$. Tian & Chen (2016) concluded that the K-H mode was unstable and evolved into filamentary flows when $2.8 \leq M_A \leq 6.2$, but the K-H vortex can fully roll up only for a very large value of M_A , say $M_A = 50$. In both of the two papers, M_A was calculated by using the initial flow velocity and Alfvén velocity along the direction of shearing flows.

Comparing our analysis in the previous paragraphs with their results, we find that the value of M_A in the jet region in our simulations are always big enough to trigger the K-H instability. But this value is not big enough in most areas in the case as shown in Figure 4 to fully roll-up the plasmas, especially in the regions near the top of the jet. Tian & Chen (2016) also found that the small scale reconnections between the rolled-up magnetic fields would destroy vortex-like structures soon after the vortex structures were formed, even for a large M_A . We notice as well many small scale current sheet

fragments due to magnetic reconnection inside the vortex-like blobs as shown in Figures 1 and 2, which also play a role in destroying the vortex blob. The appearance of these vortex-blobs last for about 8 minutes in Case I and about 6 minutes in Case II.

Zaqarashvili et al. (2015) analyzed and derived the critical conditions for the K-H instability in both the axial and the azimuthal directions of the jets. On the basis of the observation results and their theoretical models, they studied the possibilities for generating the K-H instabilities in macro-spicules, type II spicules, X-ray coronal jets and EUV jets. They concluded that the K-H instability is more likely to appear in the higher density and lower speed EUV jet, the K-H instability can still occur along the EUV jet with plasma density up to $10^{16} - 10^{17} \text{ m}^{-3}$ and velocity of 250 km s^{-1} when the axial magnetic field is about 10 G and the Alfvén speed reaches 220 km s^{-1} . For comparison, we listed several important parameters with the corresponding characteristic values obtained in this work and by Zaqarashvili et al (2015) in Table 2. We notice that the result deduced by two works are consistent with one another.

From Figures 1, 2, 5 and 7, we can see that the reconnection outflow in the main current sheet and the vortex-like structures are very different from one another in Cases I and II. The plasma velocity divergence $\nabla \cdot \mathbf{v}$ reflects the compression degree of the plasma. From the distributions of $\nabla \cdot \mathbf{v}$ in the simulation domain, we can preliminarily judge if the shock structure appears or not (Ni et al., 2017; Nóbrega-Siverio et al., 2016). We have analyzed the distributions of $\nabla \cdot \mathbf{v}$ at different times in Cases I and II. In addition to the intermediate shock at shock front SF1 as shown in Figure 5, we have recognized two fast mode shocks at shock front SF2 and shock front SF3 in the outflow region of the main current sheet in Case I with weak guide field. We only find the intermediate shock at shock front SF1 in the whole evolution process of Case II with strong guide field, and no fast mode shock appears.

We have used the MHD jump conditions as presented below (e.g., see also Ni et al. (2017)) to analyze these shocks and judge the type of shocks. In MHD jump conditions (e.g., see also Priest 2014):

$$B_{n1} = B_{n2}, \quad (14)$$

$$\rho_1 v_{n1} = \rho_2 v_{n2}, \quad (15)$$

$$\rho_1 v_{n1}^2 + p_1 + \frac{B_{t1}^2}{2\mu_0} = \rho_2 v_{n2}^2 + p_2 + \frac{B_{t2}^2}{2\mu_0}, \quad (16)$$

where subscript t represents the component which is tangential to the shock front, subscript n represents the component that is normal to the shock front, properties ahead of and behind the shock are denoted by 1 and 2. From Figures 5(a) and 5(b), we can see that the plasma is sharply heated to high temperatures behind the two fast mode shocks in Case I. But no fast mode shock occurs in Case II. However, heating that was probably caused by the compression and Joule dissipation could also be noticed (Figures 5(c) and 5(d)).

In both Cases I and II, the vortex-like structures start to break after the magnetic islands have appeared in the main current sheet as shown in Figures 1 and 2. Figure 6 shows how the vortex-like structures change before and after magnetic islands appear. One can find that the vortex-like blobs start to move toward the left bottom and break after the magnetic islands appear. Figure 6(b) shows the distribution of the kinetic energy along the jet direction at different times. As multiple reconnection X-points and magnetic islands appear in the main current sheet, the upward reconnection outflow velocity and the corresponding kinetic energy gradually decrease. When the outflows cannot provide enough kinetic energy to push the high density vortex-like blobs upward along the jet, these vortex-like blobs start to fall down. So, in addition to small scale magnetic reconnection inside the vortex like blob, magnetic islands appearing in the main current sheet is another important reason to cause the K-H instability to disappear.

As shown in Figure 6(b), the thick lines NL1 and NL2 are located along the current sheet direction at $t = 1041.3$ s before magnetic islands appear and after magnetic islands appear at $t = 1294$ s, respectively. Figures 6(c) and 6(d) show the distributions of the plasma velocity along the NL1 and NL2, they show that the outflow velocity decreases apparently after magnetic islands appear. In the turbulent reconnection process many magnetic islands of different sizes, together with the X-points, occur inside the current sheet (e.g., see also Bhattacharjee et al., 2009; Batar et al., 2011; Shen et al., 2011; Mei et al., 2012; Ni et al., 2015). The reconnection outflow bifurcates at the X-point, which makes the different sizes of magnetic islands connecting to the nearby X-point have different velocities (some of them even have opposite velocities). Therefore, these islands collide and coalesce with one another, and their motions spontaneously slow down. This issue has also been discussed previously

(e.g., see Innes et al., 2015).

As shown in Figure 7, three vortex-like blobs could be recognized clearly in Case I, but only two obvious vortex-like blobs are identified in Case II. Comparing Figure 1 with Figure 2, we notice that the magnetic island does not appear yet in the main current sheet at $t = 1186.7$ s in Case I, but several magnetic islands already appear in the main current sheet at the same time in Case II. Magnetic islands in the main current sheet of Case II appear about 3 min earlier than those in Case I. Therefore, the third vortex-like blob that was supposed to appear at the top of the jet in Case II did not show up before the two vortex-like blobs at the lower position had already been destroyed.

In order to compare with observations and previous results (Ni et al., 2017), we calculate the temperature and density dependent emission count rate, the emission count rate is calculated as $\text{ECR} = \int n^2 f(T) dl \text{ DN s}^{-1} \text{ pixel}^{-1}$, where $f(T)$ is the AIA 211 Å response function, n is the number density, and dl is the line element along the line of sight (e.g. see also Ni et al. 2017). From the AIA synthetic EUV images shown in Figure 1(e), we can see that there are three obvious vortex-like bright blobs at $t = 1044.8$ s and $t = 1186.7$ s in Case I with weak guide field, which are similar to those shown by Ni et al. (2017). As shown in Figure 2(e), the vortex-like blobs are less obvious and we can only identify two bright blobs caused by the K-H instability in Case II with strong guide field.

Ni et al. (2013) investigated the impact of guide field on the reconnection process. They showed that different guide fields result in different critical values of the Lundquist number. Magnetic islands can only appear when the Lundquist number exceeds such a critical value. Including guide field in the reconnection region changes the distributions of the plasma and the magnetic pressures. The results of this work indicate that the main current sheet reaches the critical Lundquist number earlier in the case with strong guide field. The shock structures obviously appear in the upward outflow regions of the main current sheet in Case I with weak guide field, but no apparent shock structure is found in Case II with strong guide field. It is the influence of guide field on the reconnection process as discussed above that causes the K-H instability and the vortex-like blobs to form in different fashions.

3.2 Impact of the flux emerging speed to the jet and the K-H instability

The important parameters in this work are listed in Table 1. The guide field used in Cases I, III, and IV is the same, but the emerging times in these cases were different. The total emerging time in Case III is 700 s, in Case I is 500 s and it is only 350 s in Case IV. Therefore, the flux emerging in Case IV is faster than that in Case I, and the flux emerging in Case III is the slowest one. Figure 8 shows the variations of the electromagnetic energy emerging through the bottom boundary versus time in Cases I, III, IV. The value of P_E is calculated as $P_E(t) = \iint \mathbf{P}(x, 0, t) \cdot d\mathbf{S}_{xz}$, where $\mathbf{P}(x, 0, t)$ is the Poynting flux vector through the bottom boundary and $d\mathbf{S}_{xz}$ represents the area at the bottom boundary. The direction of $d\mathbf{S}_{xz}$ is along the y -axis. Since all the variables are only functions of x, y in space and they do not change along z -direction, we then assume $d\mathbf{S}_{xz} = dxl_z\hat{\mathbf{e}}_y$ and $l_z = 100L_0$. From Figure 8, we notice that the energy emerges fastest in Case IV and the corresponding maximum of P is also the largest in three cases.

From Table 1, we notice that the jet lifetime in Case III is about 40 min which is the longest in all the cases. As shown in Figure 3, the maximum velocity along the jet direction in Case III is 295 km s^{-1} , which is slower than that in Case I. The highest temperature in Case III is 1.7 MK, which is slightly lower than that in Case I. The vortex-like blobs start to form at $t = 950 \text{ s}$ in Case III, about 150 s later than in Case I. Magnetic islands in the main current sheet of Case III start to appear at $t = 1310 \text{ s}$, 60 s later than in Case I. We also find that the jet lifetime in Case IV is about 32 min, it is the shortest one in all the cases. The maximum velocity along the jet direction is 335 km s^{-1} , which is a little bit faster than that in Case I. The maximum temperature in Case IV is 2.2 MK, which is higher than in Case I. The vortex-like blobs start to form at $t = 750 \text{ s}$, 50 s earlier than in Case I, and the magnetic islands appear at about $t = 1190 \text{ s}$, 60 s earlier than in Case I. Figure 3 also indicates that the maximum velocity along the jet direction is slower when the flux emerging speed is slower before the K-H instability initiates.

Comparing various features and behaviours of magnetic configurations in three cases, we realize that the slower the emerging speed of the magnetic field is, the longer the life time of the jet is, and the later the vortex-like blobs and the magnetic islands in the main current sheet appear. A slower emerging speed yields a lower maximum speed and lower maximum plasma temperature. From

Figure 9, we can also see that the smaller vortex-like structures are resulted from slower emerging speed.

4 CONCLUSION

On the basis of the 2D MHD coronal jet simulations by Ni et al. (2017), we included guide-field in the z -direction in this work to investigate the response corona to the new emerging flux. Detailed analysis of the K-H instability and comparisons with previous works have been conducted. We have also studied the effect of guide field and the flux emerging speed on the jet formation and the K-H instability. The main conclusions from our numerical simulations are as follow:

1. For the coronal EUV jet with the plasma density in the range from 6×10^{15} to $5 \times 10^{16} \text{ m}^{-3}$, the maximum values of magnetic field of 15 G and jet speed of 265 km s^{-1} , the Alfvén Mach number reaches 5-14 along the jet direction. The K-H instability can take place in such an EUV coronal jet. Our numerical results confirm the theoretical model and speculating results of Zaqarashvili et al. (2015).

2. The vortex-like blobs are destroyed as a result of the small-scale reconnection processes among the rolled-up magnetic field inside these blobs, as well as the slowing down of the upward reconnection outflow from the main current sheet after magnetic islands appear. A strong guide field changes the reconnection outflow pressure balance structures to prevent an apparent shock structure from being invoked, but helps magnetic islands appear earlier than in the case without guide field or with weak guide field, which further prevents the occurrence of the K-H instability and the vortex-like blob.

3. The speed of the new emerging flux affects the occurrence and development of the K-H instability as well. With the other parameters for the environment being given, the faster the flux emerges, the shorter the lifetime of the jet is, the higher the speed and the maximum temperature of the jet are, the earlier the magnetic island in the main current sheet and the K-H instability occur, and the larger and hotter the vortex-like structures are.

In this work, guide field is imbedded in the magnetic configuration of interest, and various of several important parameters, as well as the associated behaviors of the corona jet system in 2.5D have

been investigated. We expect to perform the true 3D numerical experiments in the future for looking into the formation of the flux rope (the counterpart of the magnetic island in 2D) in the main current sheet, and further studying the K-H instability in the poloidal direction as a result of the rotation of the jet.

Acknowledgements This work is supported by the NSFC Grants 11573064, 11203069, 11333007, 11303101 and 11403100; Program 973 grant 2013CBA01503; the NSFC-CAS Joint Fund U1631130; the CAS giant QYZDJ-SSW-SLH012; the Western Light of Chinese Academy of Sciences 2014; the Youth Innovation Promotion Association CAS 2017; Key Laboratory of Solar Activity grant KLSA201404. We have used the NIRVANA code v3.6 and v3.8 developed by Udo Ziegler at the Leibniz-Institut für Astrophysik Potsdam. The authors also gratefully acknowledge the computing time granted by the Yunnan Astronomical Observatories and the National Supercomputer Center in Guangzhou, the NSFC-Guangdong Joint Fund U1501501 (nscf2015-460, nscf2015-463). Some calculations of this work were performed on the Tianhe-1 supercomputer of the National Supercomputer Center in Tianjin.

References

- Alexander, D., & Fletcher, L. 1999, *Sol. Phys.*, 190, 167
Bárta, M., Büchner, J., Karlický, M., & Skála, J. 2011, *ApJ*, 737, 24
Bhattacharjee, A., Huang, Y.-M., Yang, H., & Rogers, B. 2009, *Physics of Plasmas*, 16, 112102
Chen, P. F., & Shibata, K. 2000, *ApJ*, 545, 524
Comisso, L., & Bhattacharjee, A. 2016, *Journal of Plasma Physics*, 82, 595820601
Ding, J. Y., Madjarska, M. S., Doyle, J. G., & Lu, Q. M. 2010, *A&A*, 510, A111
Forbes, T. G., & Priest, E. R. 1984, *Sol. Phys.*, 94, 315
Foullon, C., Verwichte, E., Nykyri, K., Aschwanden, M. J., & Hannah, I. G. 2013, *ApJ*, 767, 170
Innes, D. E., Guo, L.-J., Huang, Y.-M., & Bhattacharjee, A. 2015, *ApJ*, 813, 86
Jeong, H., Ryu, D., Jones, T. W., & Frank, A. 2000, *ApJ*, 529, 536
Jiang, R.-L., Fang, C., & Chen, P.-F. 2012, *ApJ*, 751, 152
Jones, T. W., Gaalaas, J. B., Ryu, D., & Frank, A. 1997, *ApJ*, 482, 230
Keppens, R., Tóth, G., Westermann, R. H. J., & Goedbloed, J. P. 1999, *Journal of Plasma Physics*, 61, 1
Kuridze, D., Zaqarashvili, T. V., Henriques, V., et al. 2016, *ApJ*, 830, 133
Li, H., Jiang, Y., Yang, J., et al. 2017, *ApJ*, 842, L20
Mei, Z., Shen, C., Wu, N., et al. 2012, *MNRAS*, 425, 2824
Moore, R. L., Cirtain, J. W., Sterling, A. C., & Falconer, D. A. 2010, *ApJ*, 720, 757
Moreno-Insertis, F., & Galsgaard, K. 2013, *ApJ*, 771, 20
Nemati, M. J., Wang, Z.-X., & Wei, L. 2017, *ApJ*, 835, 191
Nóbrega-Siverio, D., Moreno-Insertis, F., & Martínez-Sykora, J. 2016, *ApJ*, 822, 18

- Ni, L., Lin, J., & Murphy, N. A. 2013, *Physics of Plasmas*, 20, 061206
- Ni, L., Kliem, B., Lin, J., & Wu, N. 2015, *ApJ*, 799, 79
- Ni, L., Zhang, Q.-M., Murphy, N. A., & Lin, J. 2017, *ApJ*, 841, 27
- Ofman, L., & Thompson, B. J. 2011, *ApJ*, 734, L11
- Priest, E. 2014, *Magnetohydrodynamics of the Sun*, by Eric Priest, Cambridge, UK: Cambridge University Press, 2014, p177-188
- Raouafi, N. E., Patsourakos, S., Pariat, E., et al. 2016, *Space Sci. Rev.*, 201, 1
- Roy, J.-R., & Tang, F. 1975, *Sol. Phys.*, 42, 425
- Shen, Y., Liu, Y., Su, J., & Ibrahim, A. 2011, *ApJ*, 735, L43
- Shen, C., Lin, J., & Murphy, N. A. 2011, *ApJ*, 737, 14
- Shen, Y., Liu, Y., Tian, Z., & Qu, Z. 2017, *ApJ*, 851, 67
- Shibata, K., & Murdin, P. 2000, *Encyclopedia of Astronomy and Astrophysics*,
- Shibata, K., Ishido, Y., Acton, L. W., et al. 1992, *PASJ*, 44, L173
- Shibata, K., Nakamura, T., Matsumoto, T., et al. 2007, *Science*, 318, 1591
- Spitzer, L., Jr. 1962, *Physics of Fully Ionized Gases* (New York: Interscience)
- Tian, C., & Chen, Y. 2016, *ApJ*, 824, 60
- Wyper, P. F., DeVore, C. R., Karpen, J. T., & Lynch, B. J. 2016, *ApJ*, 827, 4
- Yang, L., He, J., Peter, H., et al. 2013, *ApJ*, 777, 16
- Zaqarashvili, T. V., Zhelyazkov, I., & Ofman, L. 2015, *ApJ*, 813, 123
- Zhang, Q. M., & Ji, H. S. 2014, *A&A*, 567, A11
- Zhang, Q. M., Ji, H. S., & Su, Y. N. 2016, *Sol. Phys.*, 291, 859
- Zhang, Y., & Zhang, J. 2017, *ApJ*, 834, 79
- Ziegler, U. 2011, *Journal of Computational Physics*, 230, 1035
- Ziegler, U. 2008, *Computer Physics Communications*, 179, 227

Table 1 The important parameters in different cases in our simulations. b_0 is the initial background magnetic field, t_{life} the lifetime of the jet, $v_{||\text{max}}$ is the maximum velocity along the jet direction, t_v is the time when the vortex structure starts to appear, t_i is the time when the magnetic island starts to appear, N is the number of vortex structures, T_{max} is the maximum temperature in the jet.

Case	t_1 (s)	b_z	t_{life} (min)	$v_{ \text{max}}$ (km/s)	t_v (s)	N	t_i (s)	T_{max} (MK)
I	500	$0.05b_0$	37	320	800	2	1250	1.8
II	500	b_0	33	275	850	2	1080	1.6
III	700	$0.05b_0$	40	295	950	3	1310	1.7
IV	350	$0.05b_0$	32	335	750	3	1190	2.2

Table 2 Comparies of values of some important parameters studied by Zaqrarshvili et al (2015) and by us in Case I. Our results are selected at $t = 784.3$ s in the simulation just before the K-H instability takes place. Both the jet speed and the Alfvén speed are along the jet direction.

Parameters	Zaqrarshvili's	Case I (average)	CaseI (maximum)
Magnetic field(G)	10	5	15
Alfvén speed(km/s)	220	50	250
Jet speed (km/s)	250	160	265
Density (m^{-3})	$10^{16} - 10^{17}$	2.8×10^{16}	5×10^{16}

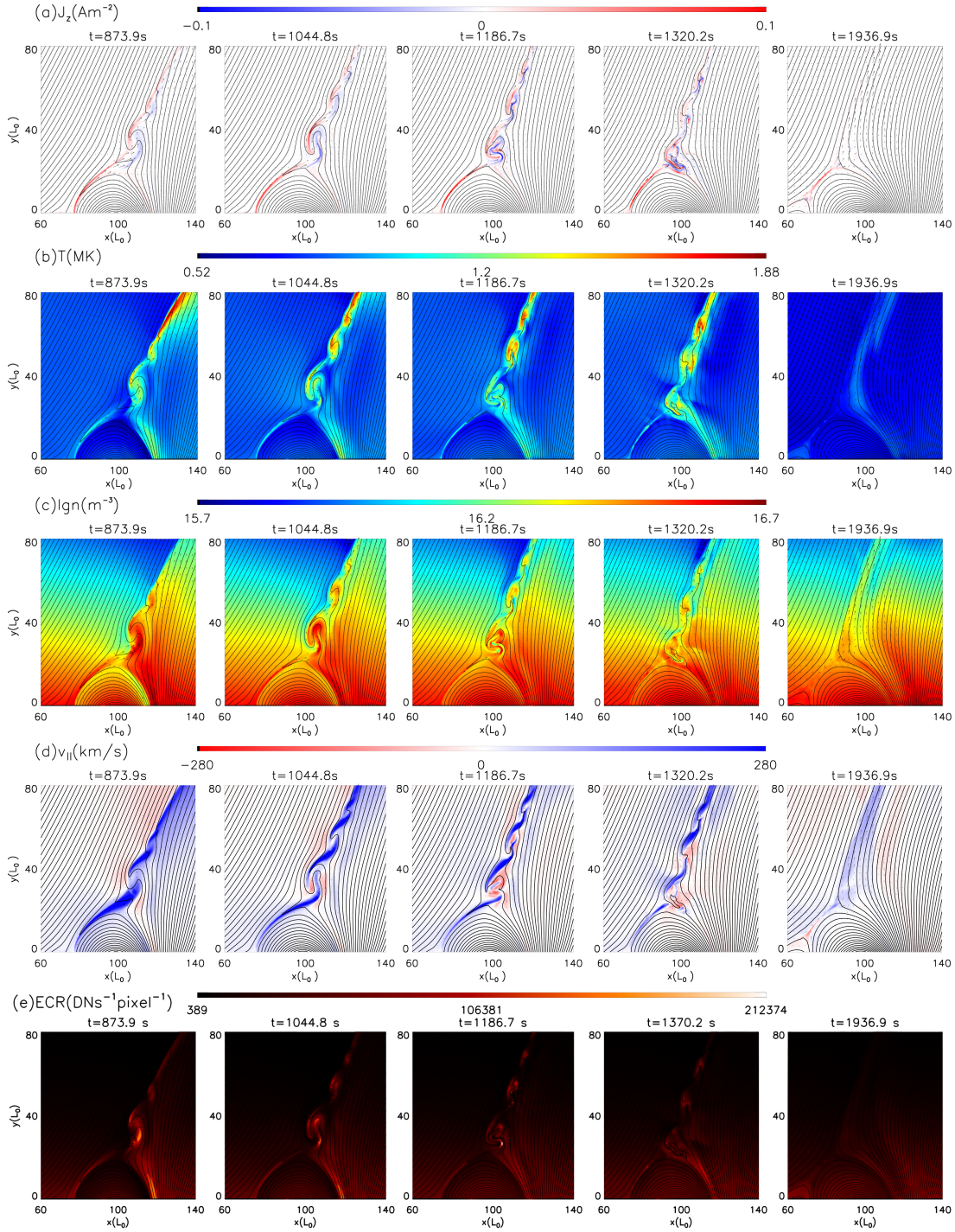


Fig. 1 Distributions of different variables at five different times in Case I, (a) current density, J_z , (b) temperature, T , (c) logarithm of plasma number density, $\lg n$, (d) velocity along the jet direction, $v_{||max}$. (e) The distributions of the emission count rate in the AIA 211 Å channel at five different times in Case I. Continuous black curves represent the magnetic fields and the black arrows represent the velocity vector in each panels.

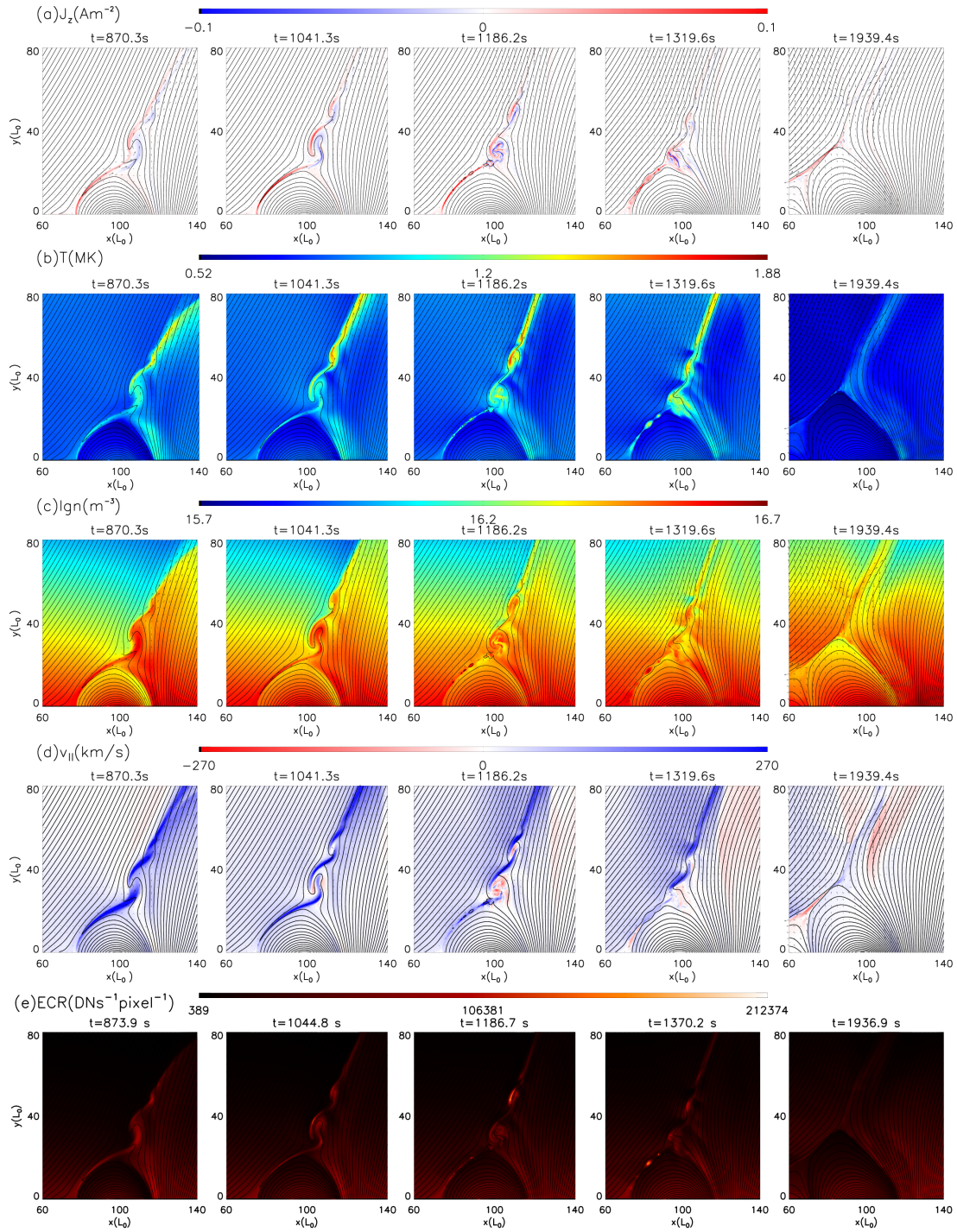


Fig. 2 Same as Figure 1 for Case II.

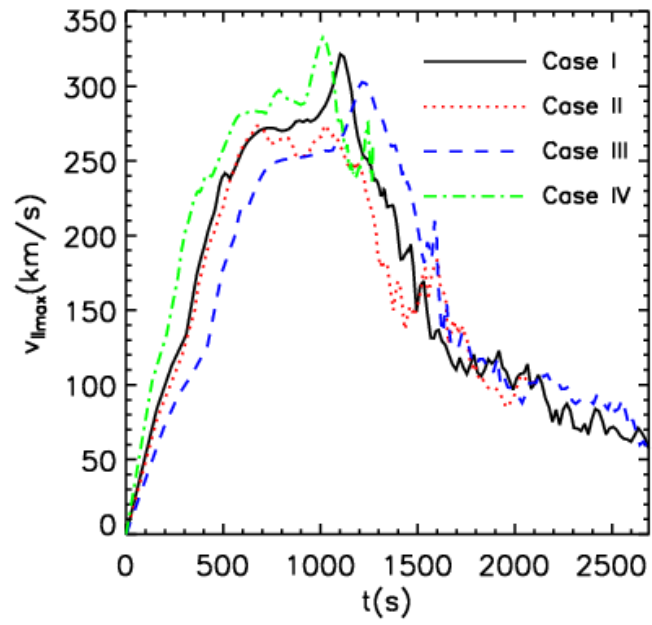


Fig. 3 The maximum velocities along the jet direction versus time for four cases.

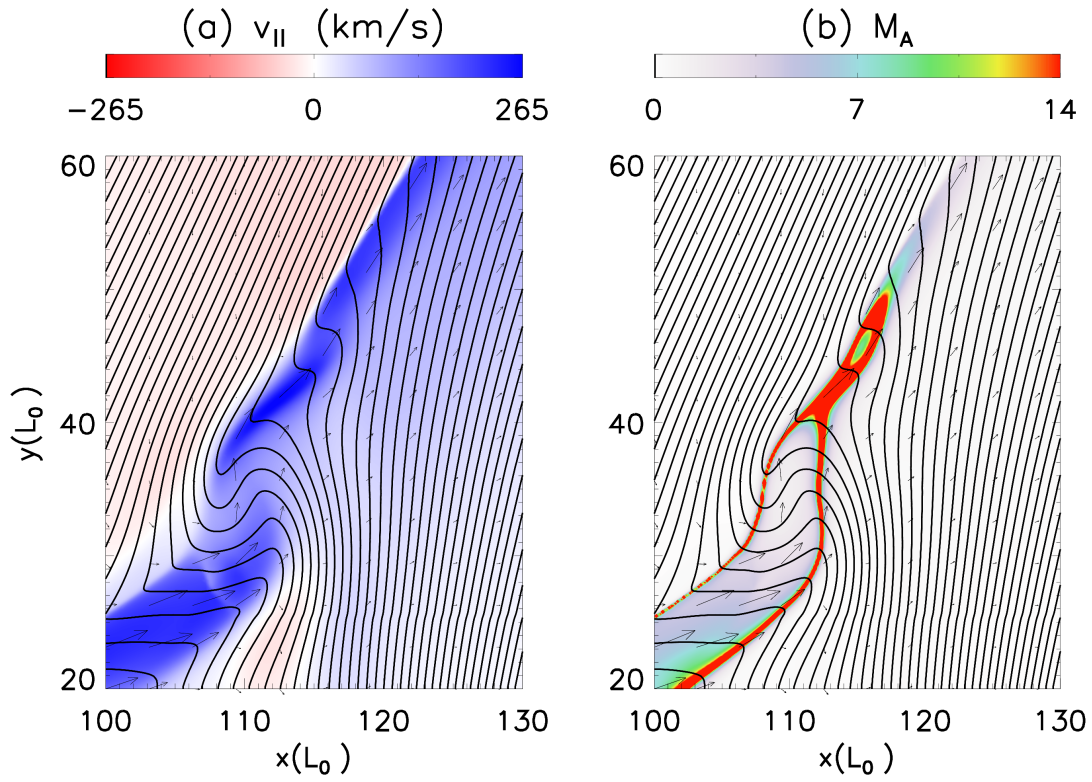


Fig. 4 Distributions of the velocity and M_A along the jet direction for Case I at $t = 784.3$ s.

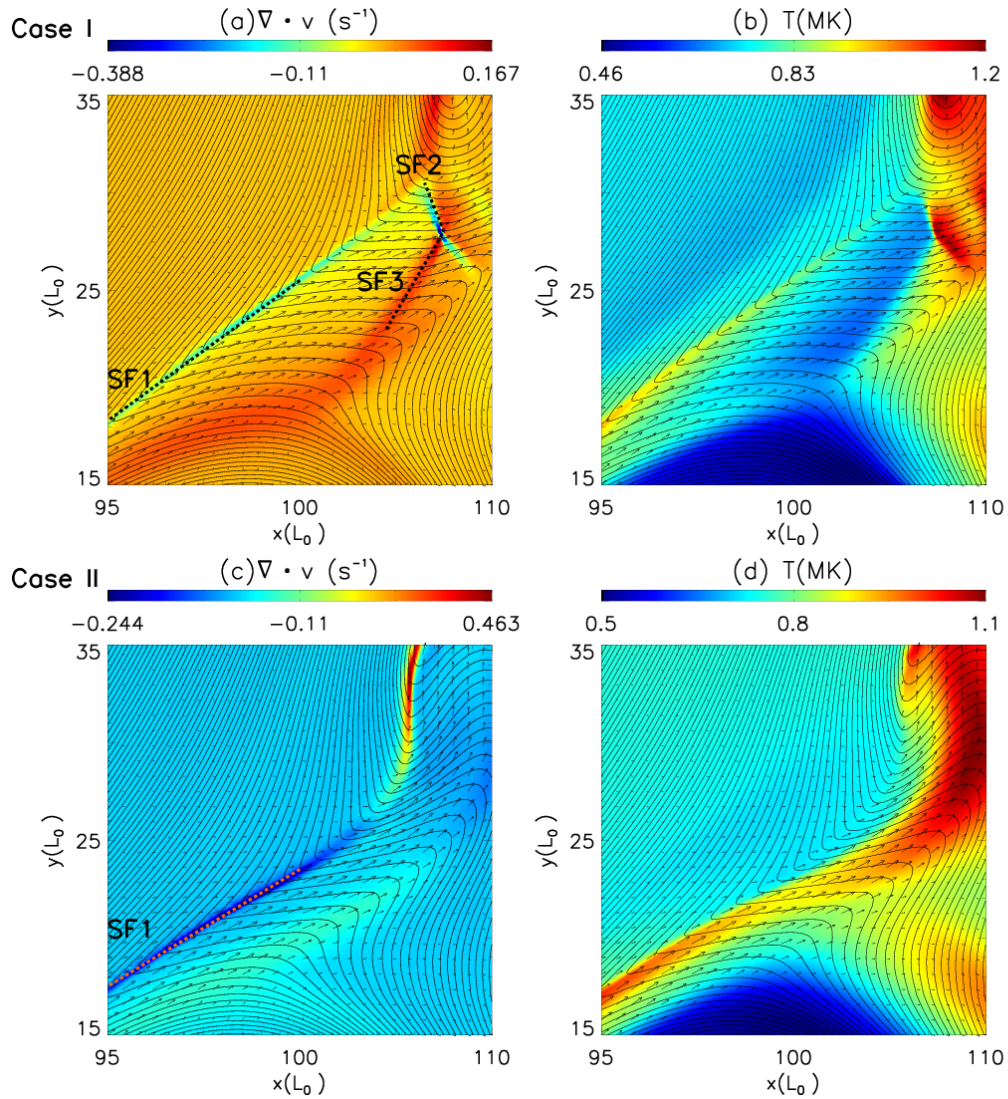


Fig. 5 Distributions of the velocity divergence (a) and temperature (b) in the reconnection outflow region of the main current sheet at $t = 801.7$ s in Case I ; the same for Case II in panels (c) and (d) at $t = 794.8$ s.

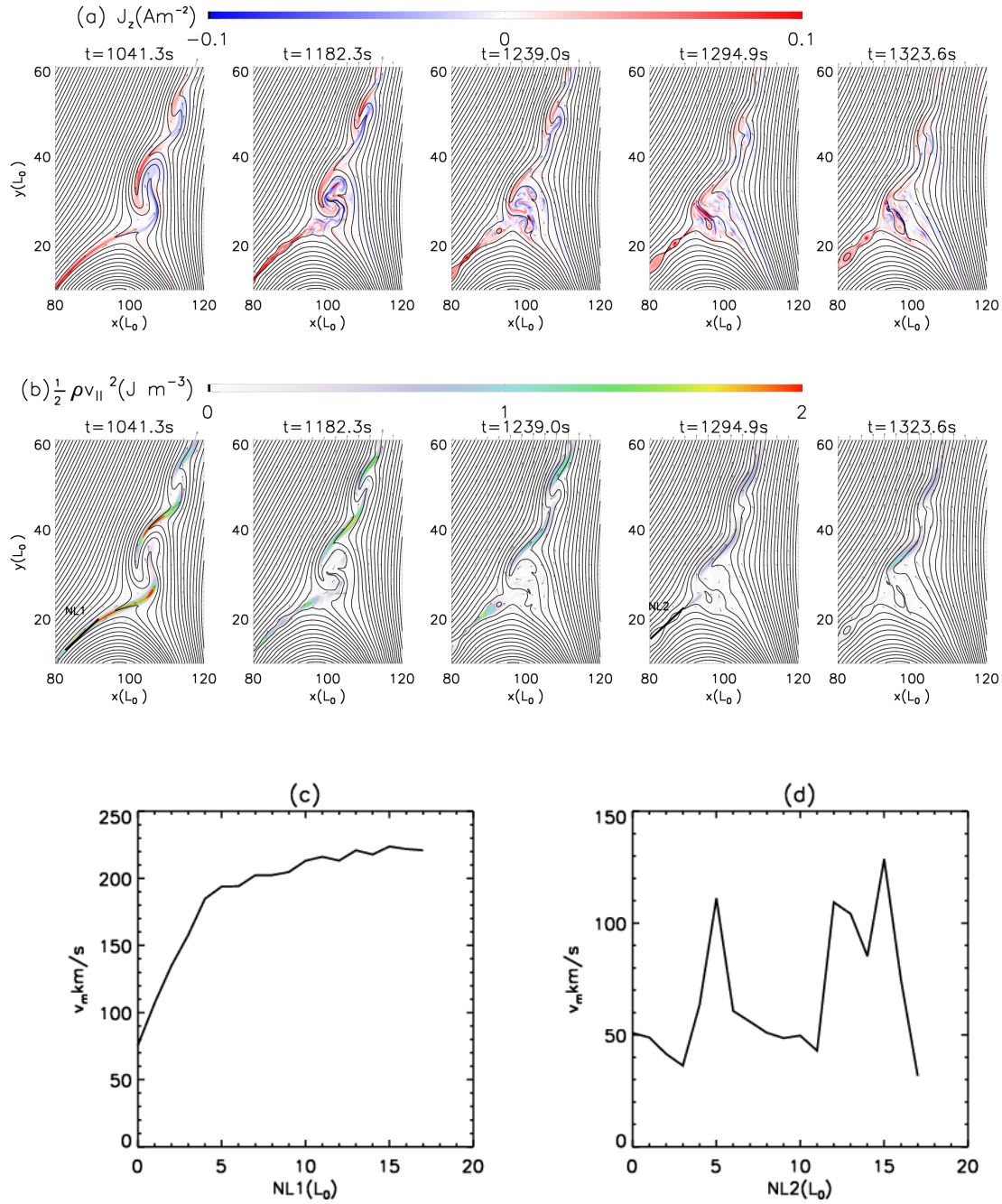


Fig. 6 (a) Distributions the current density, J_z , (b) the kinetic energy $\rho v_{\parallel}^2/2$ along the jet direction before and after the magnetic island in the main current sheet appears for Case II, (c) velocity along the current sheet direction NL1 at $t = 1041.3\text{s}$, (d) velocity along the current sheet direction NL2 at $t = 1294.9\text{s}$.

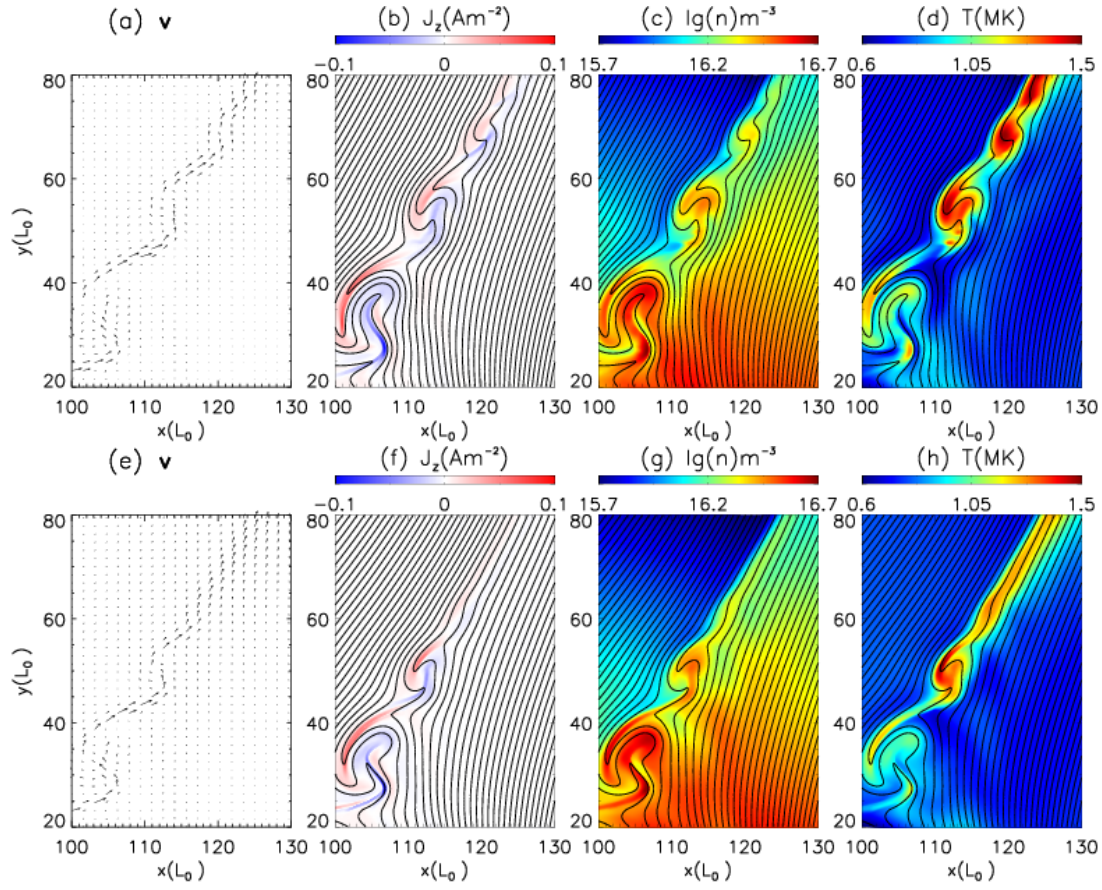


Fig. 7 The distribution of velocity vector, current density J_z , logarithm of plasma number density $\lg n$, temperature T . Panels (a), (b), (c), and (d) are for Case I at $t = 1082$ s; and panels (e), (f), (g), and (h) are for Case II at $t = 1079$ s.

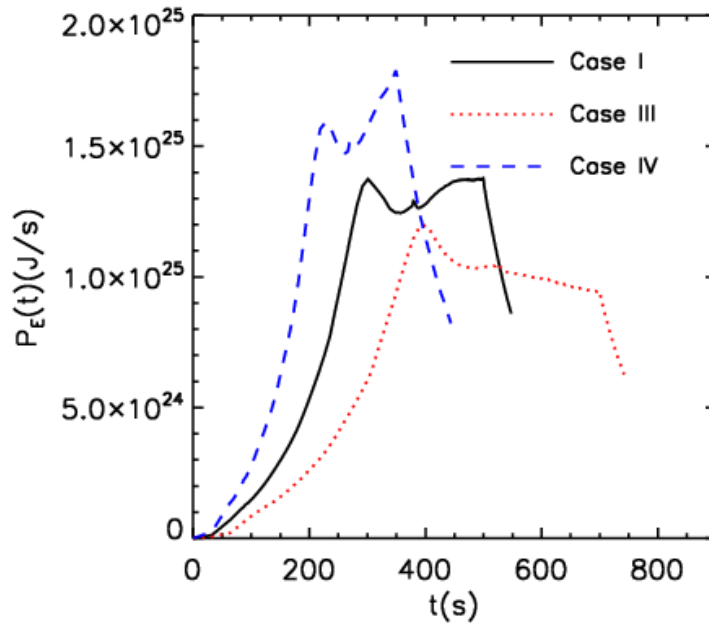


Fig. 8 Variations of the electromagnetic energy emerging through the bottom boundary versus time in Cases I, III, IV.

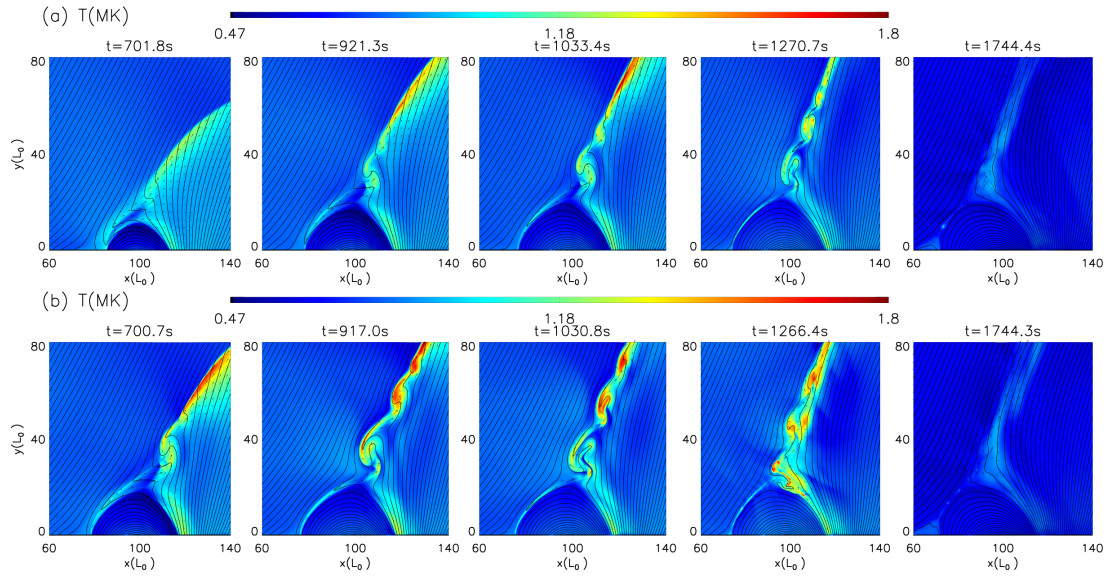


Fig. 9 Distributions of the temperature T at five different times for Case III (upper row) and Case IV (bottom row).